Supporting Information

Constructing electron-rich interface over Sb/Nb$_2$CT$_x$-MXene heterojunction for enhanced electrocatalytic nitrogen reduction

Xingchuan Li[#], Yaojing Luo[#], Qingqing Li, Yali Guo, Ke Chu*

School of Materials Science and Engineering, Lanzhou Jiaotong University, Lanzhou 730070, China

*Corresponding author. E-mail address: chukelut@163.com (K. Chu)

[#] These authors contributed equally to this work.

Experimental Section

Synthesis of Sb/Nb$_2$CT$_x$

All the chemicals were used as received without further purification. The Sb/Nb$_2$CT$_x$ was synthesized by a facile in-situ chemical reduction method[1]. To prepare Nb$_2$CT$_x$, 1 g of Nb$_2$AlC powder was added to 10 ml of HF solution (50 wt%) under stirring at 60 ^{o}C for 90 h. The resulting suspension was centrifugally washed several times until the pH of the supernatant was ~6. The solution was freeze-dried to obtain Nb$_2$CT$_x$. To prepare Sb/Nb$_2$CT$_x$, 50 mg of Nb$_2$CT$_x$ was dispersed in 50 mL of absolute ethyl alcohol under ultrasonication for 2 h to acquire a uniform suspension. Then, 40 mg of NaBH$_4$ was quickly added and stirred until completely dissolved. Afterwards, 60 mg of SbCl$_3$ were dissolved in 30 mL of absolute ethyl alcohol, and added drop by drop in above Nb$_2$CT$_x$ suspension with magnetic stirring. After reaction for 10 h, the obtained black precipitates were collected by centrifugation, washed with deionized water and ethanol several times and then annealed in a quartz tube furnace at 400 ^{o}C for 2 h under argon atmosphere, obtaining the Sb/Nb$_2$CT$_x$.

Electrochemical experiments

Electrochemical measurements were performed on a CHI-760E electrochemical workstation using a three-electrode system comprising reference Ag/AgCl (saturated KCl) electrode, counter electrode (graphite rod), and the working electrode (catalyst coated on carbon cloth (CC)). All potentials were referenced to reversible hydrogen electrode (RHE) by following equation: E_{RHE} (V)=$E_{Ag/AgCl}$+0.197+0.059×pH. The CC (1 × 1 cm^2) was pretreated by soaking it in 0.5 M H$_2$SO$_4$ for 12 h, and then washed with several times and dried at 60 ^{o}C for 24 h. The working electrode was prepared by the following procedure: dispersing 1 mg catalyst and 5 μL of Nafion (5 wt%) in 95 μL of ethyl alcohol led to the 100 μl of the homogeneous ink. Then 20 μL of catalyst ink was loaded on a 1×1 cm^2 CC substrate and dried under ambient condition. The NRR tests were carried out using an H-type two-compartment electrochemical cell separated by a Nafion 211 membrane[2-4]. The Nafion membrane was heat-treated in 5% H$_2$O$_2$, 0.5 M H$_2$SO$_4$, and deionized water for 1 h, respectively. After rinsing in

water thoroughly, the Nafion membrane was immersed in deionized water for further use. During each electrolysis, ultra-high-purity N_2 gas (99.999%) was continuously purged into the cathodic chamber at a flow rate of 20 mL min^{-1}. After each NRR electrolysis, the produced NH_3 and possible N_2H_4 were quantitatively determined by the indophenol blue method[5], and approach of Watt and Chrisp[6], respectively. The detailed processes are provided in our previous reports[7-9].

Nuclear magnetic resonance measurement

^{1}H nuclear magnetic resonance (NMR) measurement was carried out using $^{14}N_2$ and $^{15}N_2$ as the feed gas. Prior to NMR measurement, $^{14}N_2/^{15}N_2$ gases were purified by an acid trap (0.05 M H_2SO_4) to eliminate the NO_x and NH_3 contaminants [10]. After NRR electrolysis, 4 mL of electrolyte was removed from the electrochemical reaction vessel, which was concentrated to 1 mL and further acidized to pH 2. The obtained electrolyte was mixed with 0.1 mL of deuterium oxide (D_2O) containing 100 ppm of dimethyl sulphoxide (DMSO) and 70 μL of D_2O for NMR spectroscopy measurement (500 MHz Bruker superconducting-magnet NMR spectrometer).

Characterizations

X-ray diffraction (XRD) pattern was conducted on a Rigaku D/max 2400 diffractometer. Scanning electron microscopy (SEM) was performed on a JSM-6701 microscope. Transmission electron microscopy (TEM), high-resolution transmission electron microscopy (HRTEM) and high-angle annular dark-field scanning transmission electron microscopy (HAADF-STEM) were conducted on a Tecnai G^2 F20 microscope. X-ray photoelectron spectroscopy (XPS) analysis was carried out on a PHI 5702 spectrometer. Temperature-programmed desorption (TPD) profiles were performed on a Chem-BET 3000 (Quantachrome) apparatus. Ion chromatogram measurements were conducted on a Dionex ICS-2000 ion chromatographs. The UV-vis absorbance measurements were measured using a MAPADA P5 spectrophotometer.

Calculation details

Spin polarized density functional theory (DFT) calculations were performed using the Cambridge sequential total energy package (CASTEP) package[11]. The

exchange-correlation interactions were treated within the generalized gradient approximation (GGA) in the form of the Perdew−Burke−Ernzerhof (PBE) functional. DFT-D method was employed to calculate the van der Waals interactions. Energy cut off of 550 eV and applicable k-points of 3×3×1 were used. During the geometry optimization, the convergence criteria of force and energy were set to be 0.01 eV Å^{-1} and 2.0×10^{-5} eV, respectively. The Sb/Nb$_2$CT$_x$ model was built by supporting Sb nanocluster on single-layered O-terminated Nb$_2$CT$_x$ (3×3×1 supercell). A vacuum region of 15 Å was used to separate adjacent slabs.

The adsorption energy (ΔE) is defined as [12]

$$\Delta E = E_{ads/slab} - E_{ads} - E_{slab} \tag{1}$$

where $E_{ads/slab}$, E_{ads} and E_{slab} are the total energies for adsorbed species on slab, adsorbed species and isolated slab, respectively.

The Gibbs free energy (ΔG, 298 K) of reaction steps is calculated by [12]:

$$\Delta G = \Delta E + \Delta ZPE - T\Delta S \tag{2}$$

where ΔE is the adsorption energy, ΔZPE is the zero point energy difference and $T\Delta S$ is the entropy difference between the gas phase and adsorbed state. The entropies of free gases were acquired from the NIST database.

The p-band center (ε_p) is calculated based on projected density of states (PDOS) and following equation [13]:

$$\varepsilon_p = \frac{\int_{-10}^{10} n_p(\varepsilon)\varepsilon d_\varepsilon}{\int_{-10}^{10} n_p(\varepsilon)d_\varepsilon} \tag{3}$$

where ε is the energy in eV, and $n_p(\varepsilon)$ is the electron density.
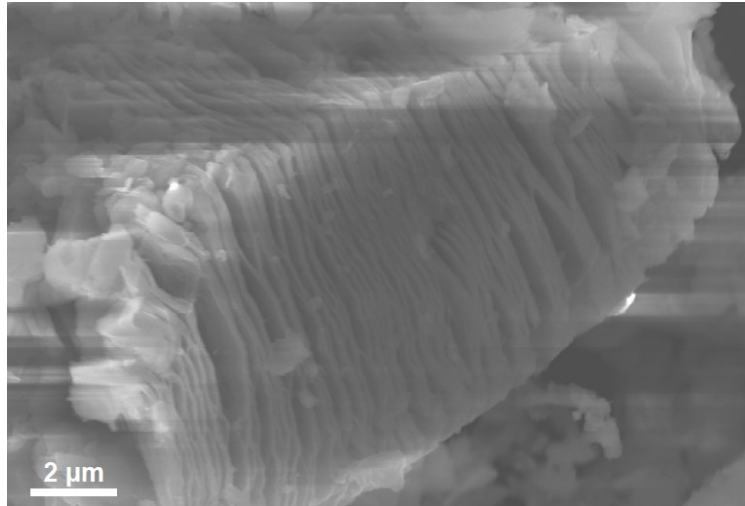
Fig. S1. SEM image of as-prepared Nb_2CT_x.
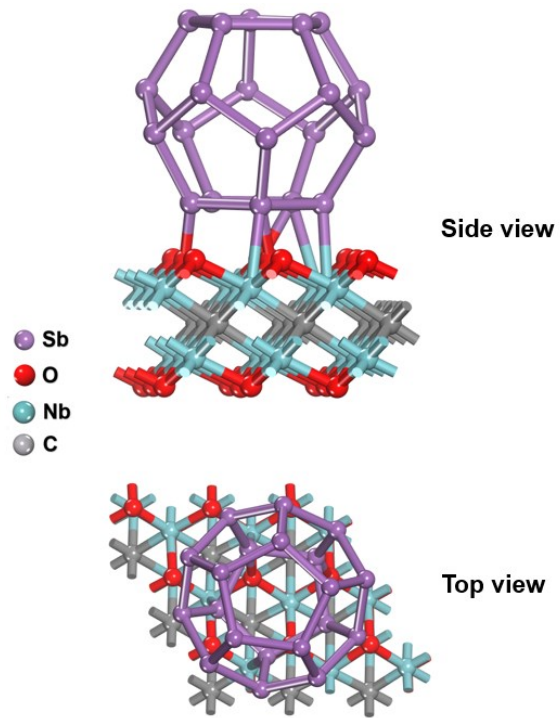
Fig. S2. Side-view and top-view images of Sb/Nb$_2$CT$_x$ heterojunction.
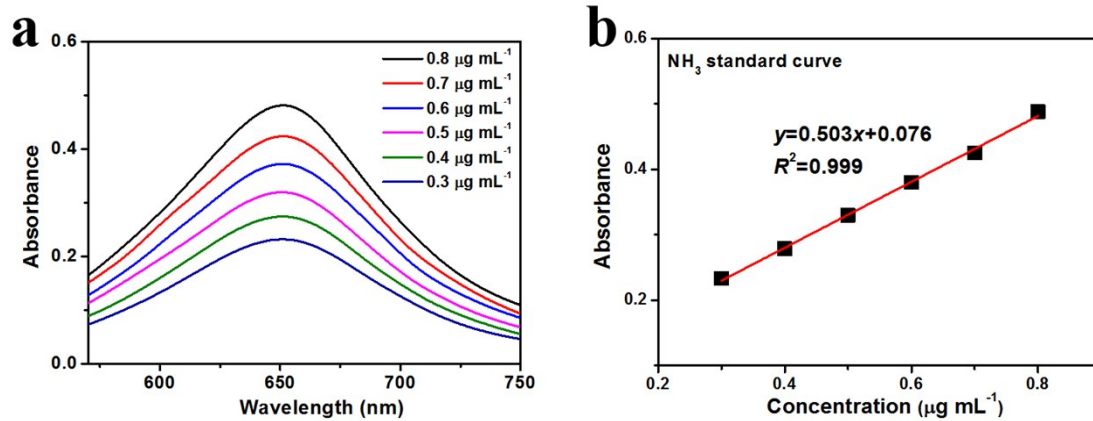
Fig. S3. (a) UV-vis absorption spectra of indophenol assays with NH₄Cl after incubated for 2 h at ambient conditions. (b) Calibration curve used for calculation of NH₃ concentrations.
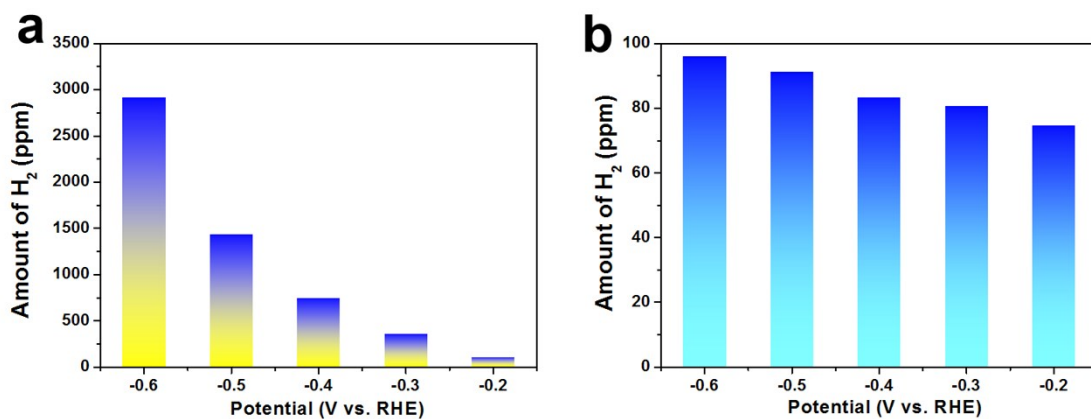
Fig. S4. (a) Amounts of produced H_2 and (b) corresponding FE of H_2 yield at various potentials.

The FE for H_2 yield can be calculated by [14]

$$FE\ (\%) = \frac{2 \times F \times n}{Q} \times 100\% \qquad (4)$$

where Q is the quantity of applied electricity. F is the Faraday constant, n is the actually produced H_2 (mol) obtained by gas chromatography (GC) analysis[15]. Based on the FE data (for H_2 production) with the FE for NH_3 selectivity (Fig. 3c), the unaccounted values are possibly derived from the dynamic hydrogen adsorption on the catalyst, the capacitance of the support and the uncontrollable experimental error[16].
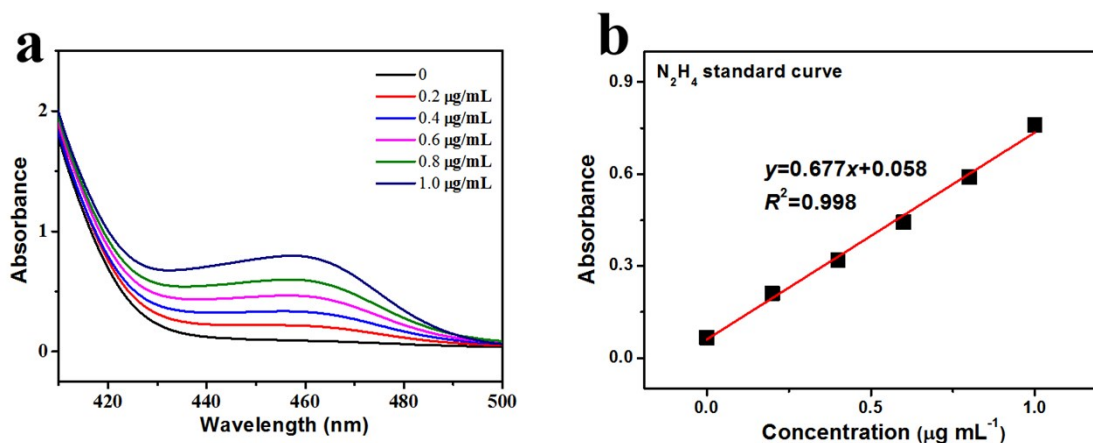
Fig. S5. (a) UV-vis absorption spectra of N_2H_4 assays after incubated for 20 min at ambient conditions. (b) Calibration curve used for calculation of N_2H_4 concentrations.
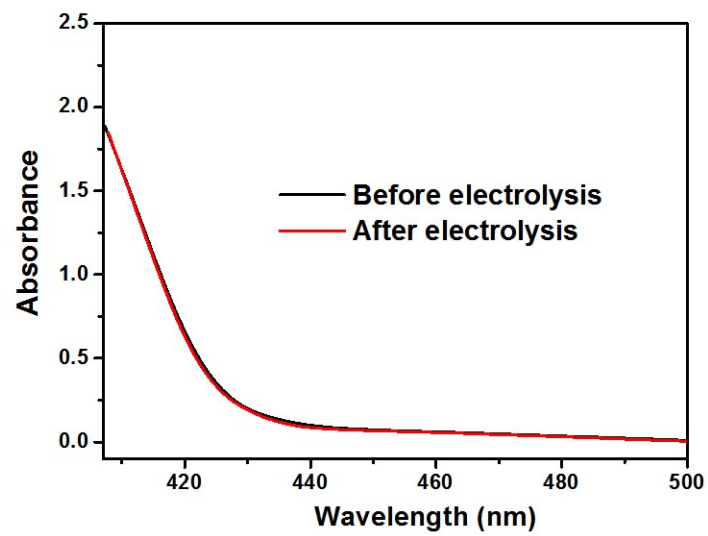
Fig. S6. UV-vis spectra of the electrolytes (stained with the chemical indicator based on the method of Watt and Chrisp) before and after 2 h of NRR electrolysis at -0.4 V.
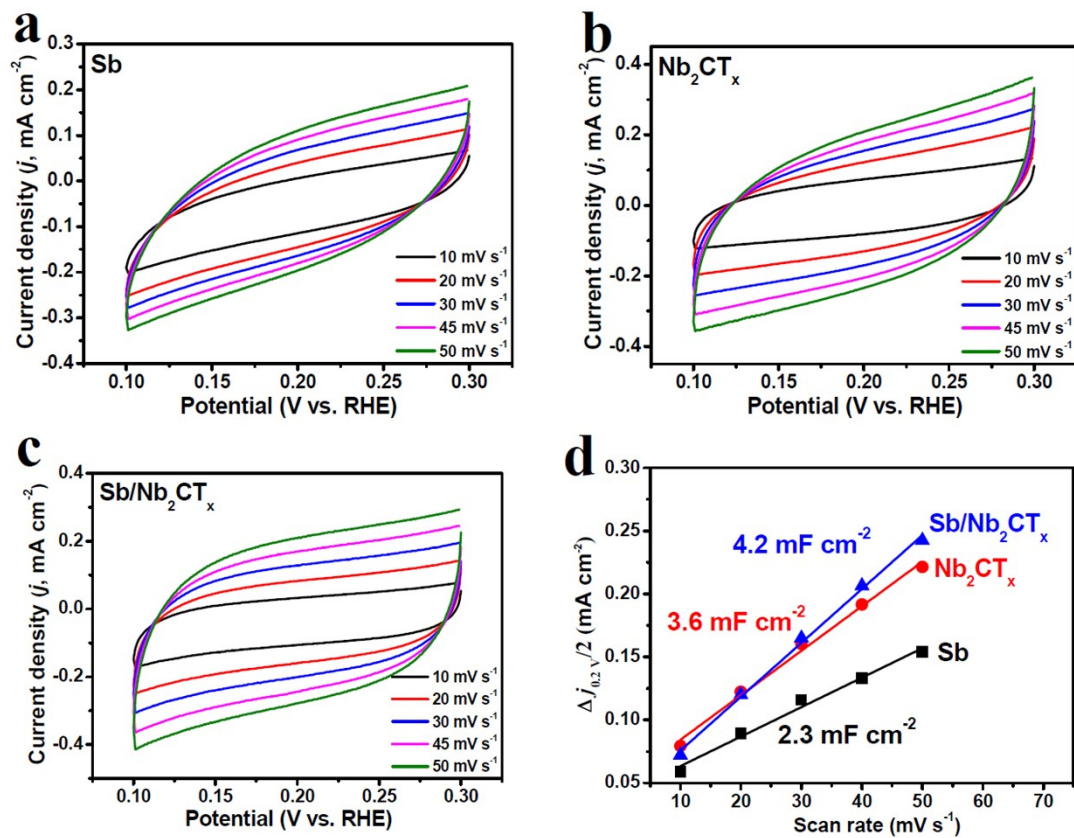
Fig. S7. Cyclic voltammetry curves of (a) Sb, (b) Nb_2CT_x and (c) Sb/Nb_2CT_x at various scan rates of 10-50 mF cm^{-1}, and (d) their corresponding plots of current density differences $\Delta j/2$ vs. scan rate at 0.20 V vs. RHE.
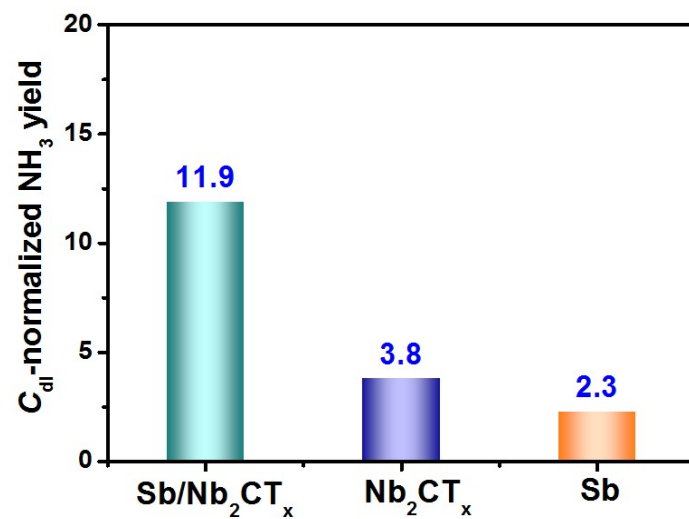
Fig. S8. Double-layer capacitance (C_{dl}) normalized NH_3 yields of Sb, Nb_2CT_x and Sb/Nb_2CT_x at -0.4 V.
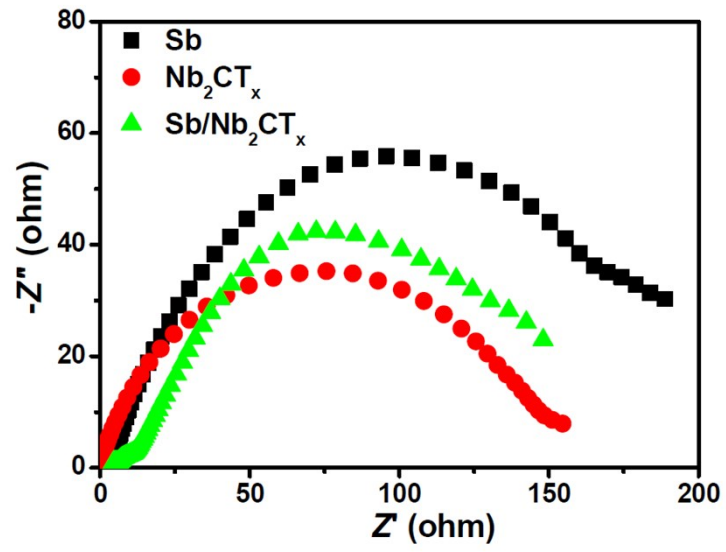
Fig. S9. Electrochemical impendence spectra of Sb, Nb_2CT_x and Sb/Nb_2CT_x.
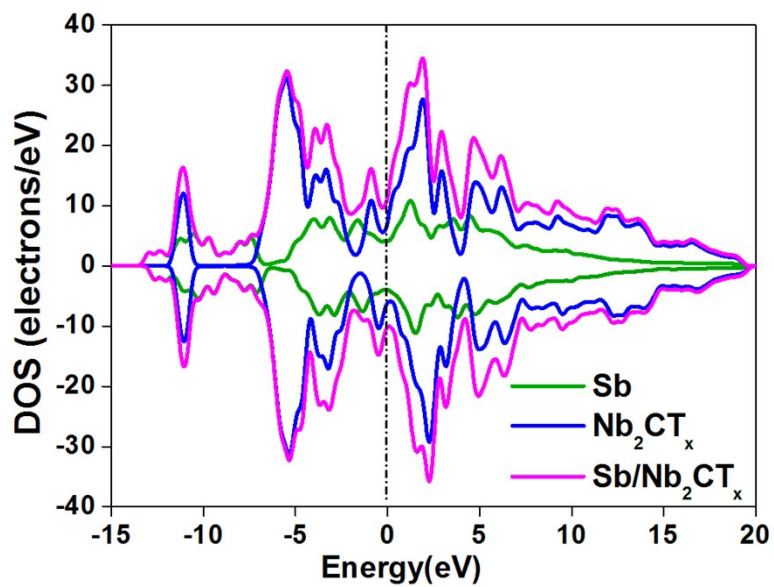
Fig. S10. DOS of Sb, Nb_2CT_x and Sb/Nb_2CT_x.
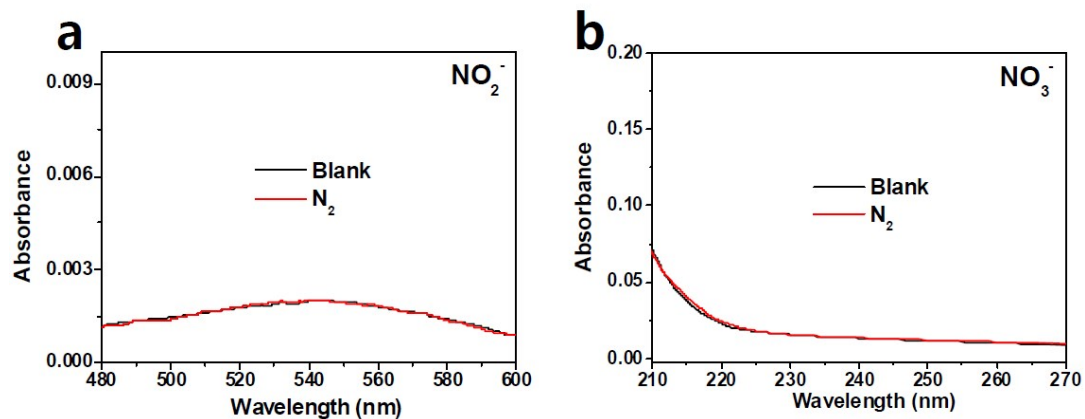
Fig. S11. Determination of NO_x contaminations in N_2 gas: (a, b) UV-vis absorption spectra for the determination of (a) NO_2^- and (b) NO_3^- contaminants in blank (deionized water) and tested solution (continuously passing N_2 gas through 20 ml of deionized water at a flow rate of 20 sccm for 2 h). The calibrate curves for calculation of NO_2^- and NO_3^- concentrations are given in the following Figs. S13-S14.
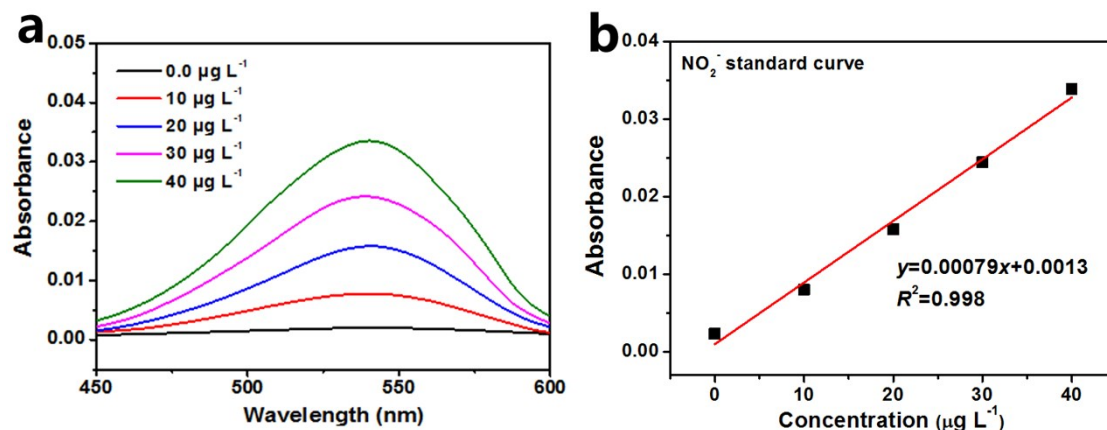
Fig. S12. (a) UV-vis absorption spectra of pink azo dye assays with KNO_2 after incubated for 10 min at ambient conditions. (b) Calibration curve used for calculation of NO_2^- concentrations. The detection of nitrite (NO_2^-) is based on the Griess-llosvay reaction[17], in which NO_2^- reacts with detection reagent, yielding pink azo dye that can be spectrophotometrically analyzed by visible light at 540 nm.
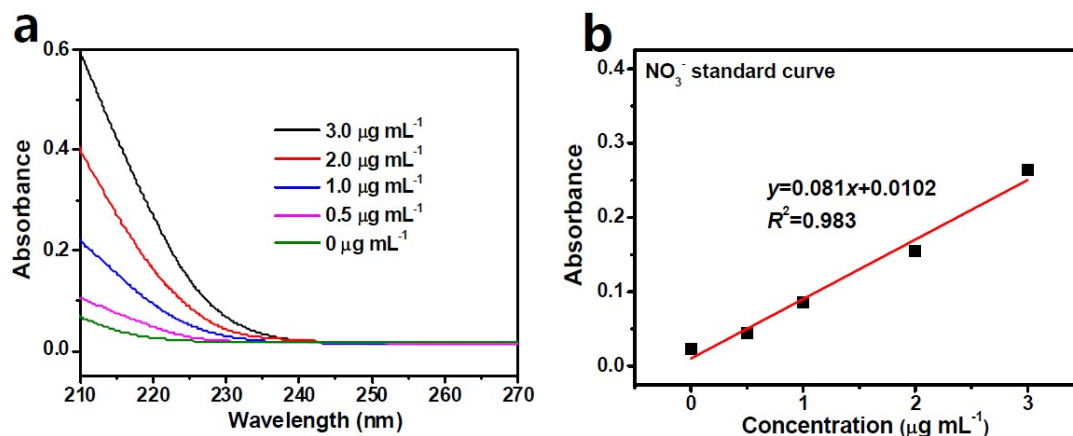
Fig. S13. (a) UV-vis absorption spectra of KNO_3 assays after incubated for 5 min at ambient conditions. (b) Calibration curve used for calculation of NO_3^- concentrations. The detection of nitrate (NO_3^-) is based on its UV absorption at visible light of 220 nm where the absorbance value is proportional to its concentration[17].
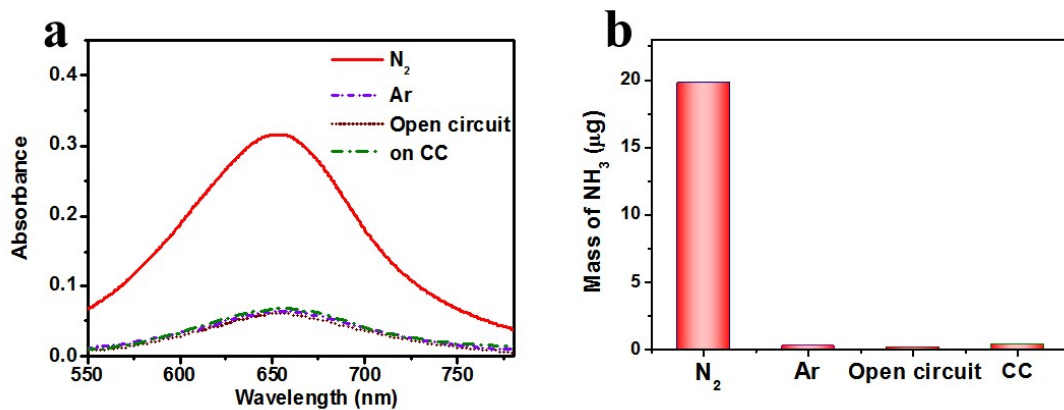
Fig. S14. (a) UV-vis absorption spectra of working electrolytes after 2 h of electrolysis in Ar-saturated solutions on Sb/Nb$_2$CT$_x$ at -0.4 V, N$_2$-saturated solution on Sb/Nb$_2$CT$_x$ at open circuit, and N$_2$-saturated solution on pristine CC at -0.4 V. (b) Corresponding mass of produced NH$_3$.
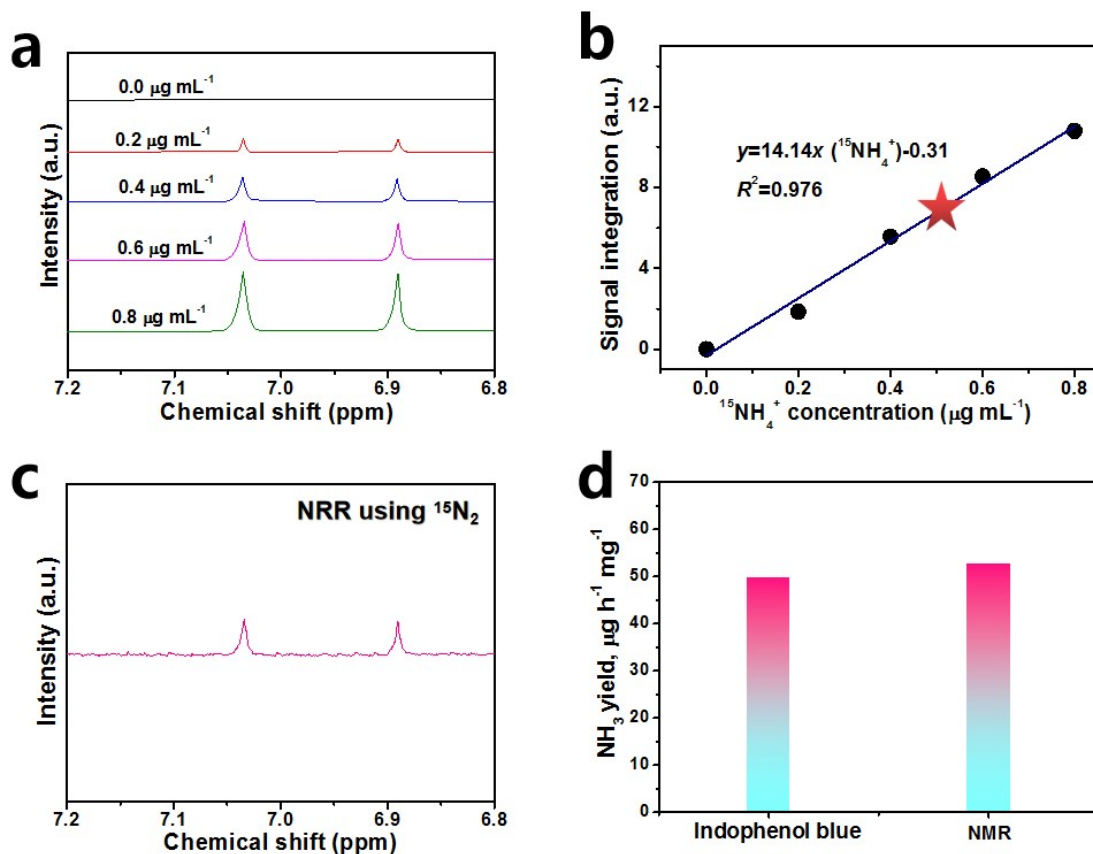
Fig. S15. (a) ^{1}H NMR spectra of $^{15}NH_4^+$ standard samples with different concentrations, and (b) corresponding calibration curve of $^{15}NH_4^+$ concentration vs. peak area, red star represents the $^{15}NH_4^+$ concentration derived from the NRR fed by $^{15}N_2$ over Sb/Nb$_2$CT$_x$ at -0.4 V for 2 h (c). (d) Comparison of the NH$_3$ yield of Sb/Nb$_2$CT$_x$ obtained from indophenol blue and NMR methods.
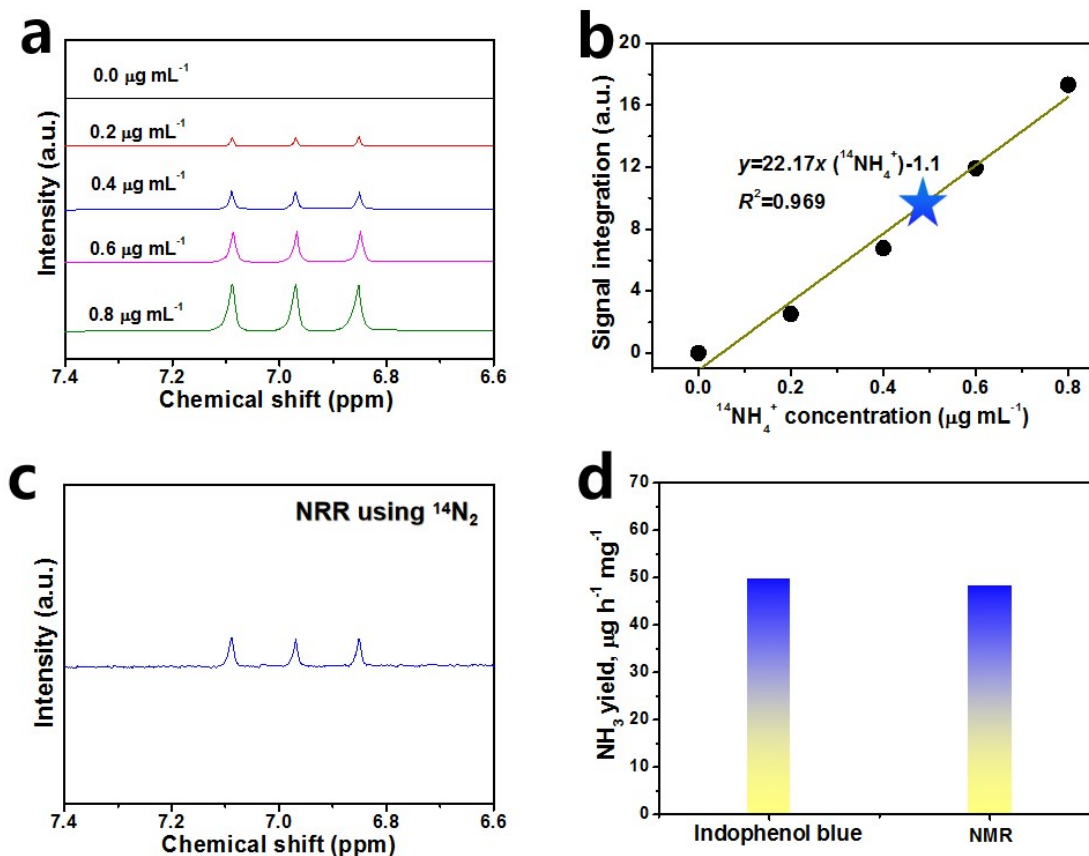
Fig. S16. (a) ^{1}H NMR spectra of $^{14}NH_4^+$ standard samples with different concentrations, and (b) corresponding calibration curve of $^{14}NH_4^+$ concentration vs. peak area, blue star represents the $^{14}NH_4^+$ concentration derived from the NRR fed by $^{14}N_2$ over Sb/Nb$_2$CT$_x$ at -0.4 V for 2 h (c). (d) Comparison of the NH$_3$ yield of Sb/Nb$_2$CT$_x$ obtained from indophenol blue and NMR methods.
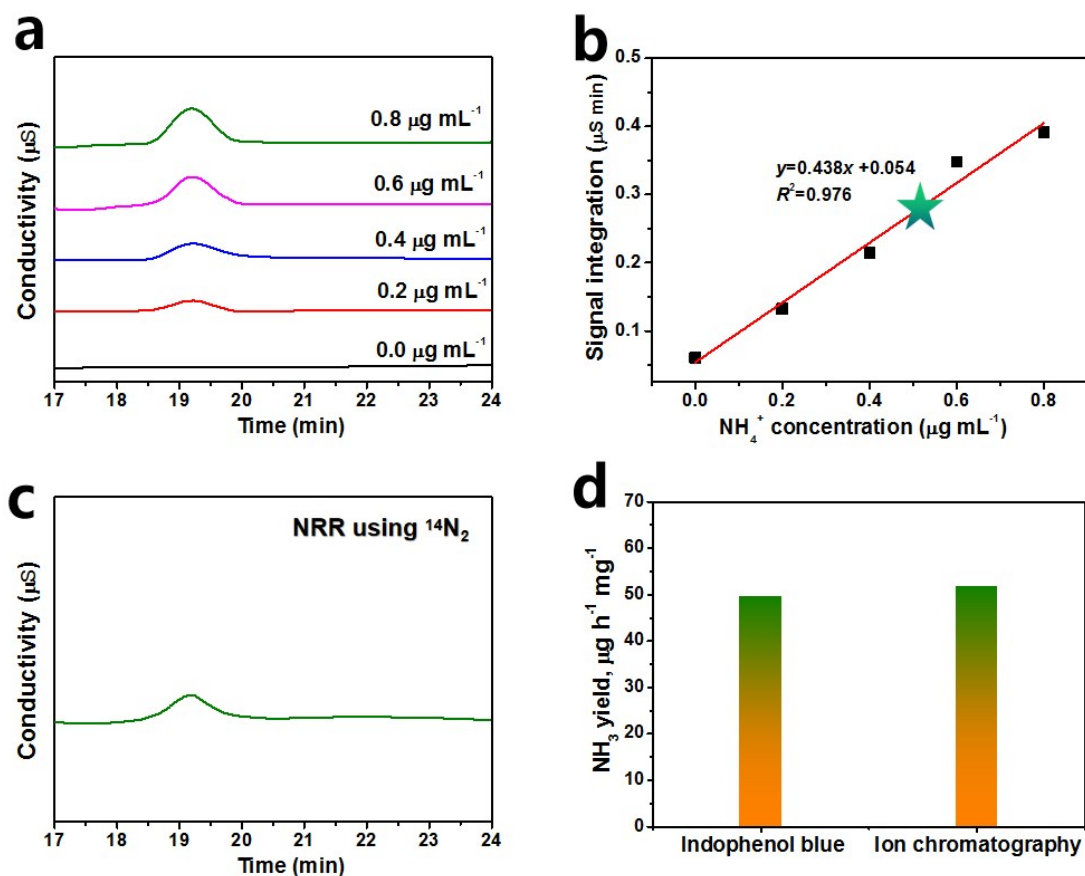
Fig. S17. (a) Ion chromatogram spectra of $^{14}NH_4^+$ standard samples with different concentrations, and (b) corresponding calibration curve of $^{14}NH_4^+$ concentration vs. peak area, green star represents the $^{14}NH_4^+$ concentration derived from the NRR fed by $^{14}N_2$ over Sb/Nb_2CT_x at -0.4 V for 2 h (c). (d) Comparison of the NH_3 yield of Sb/Nb_2CT_x obtained from indophenol blue and ion chromatogram methods.
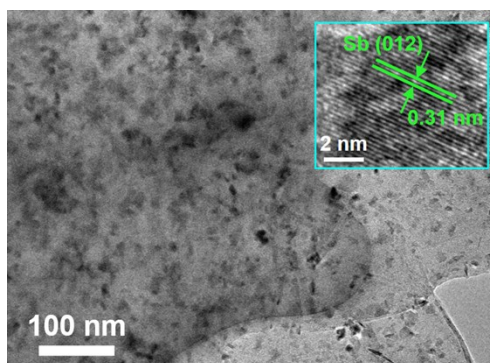
Fig. S18. TEM and HRTEM (inset) images of Sb/Nb$_2$CT$_x$ after stability test.
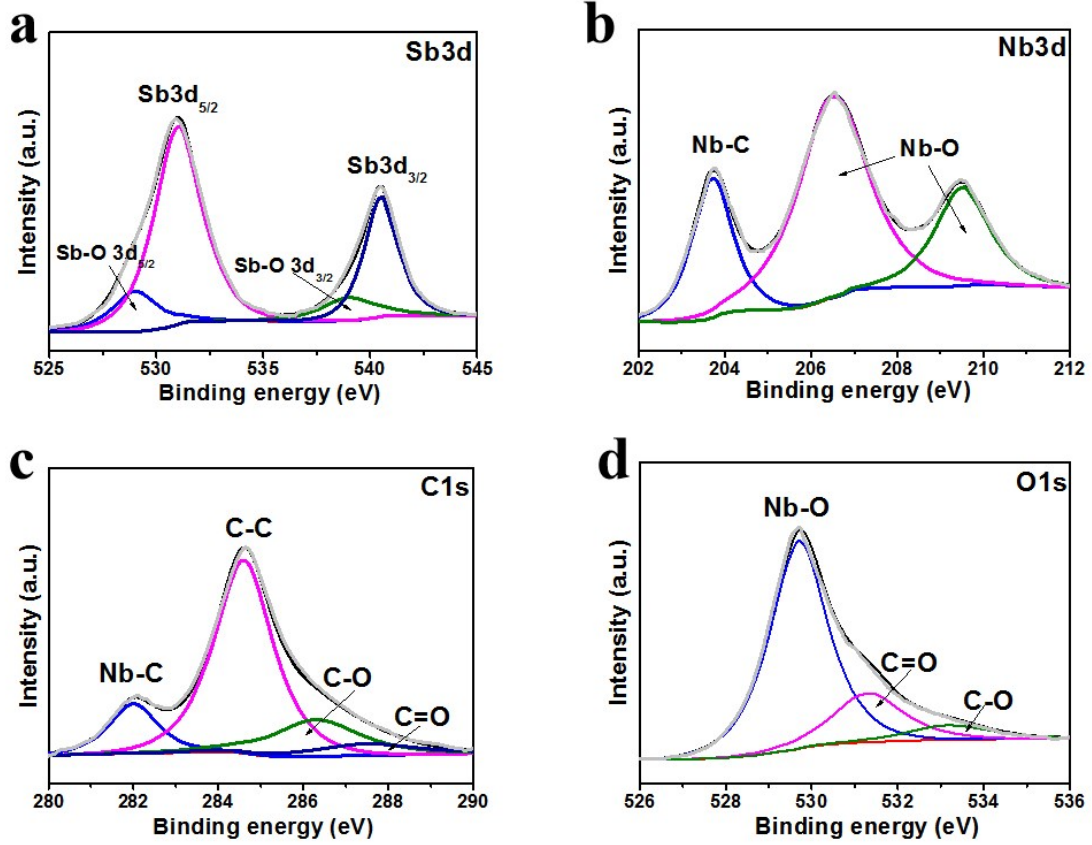
Fig. S19. XPS spectra of Sb/Nb$_2$CT$_x$ after stability test: (a) Sb3d; (b) Nb3d; (c) C1s; (d) O1s.
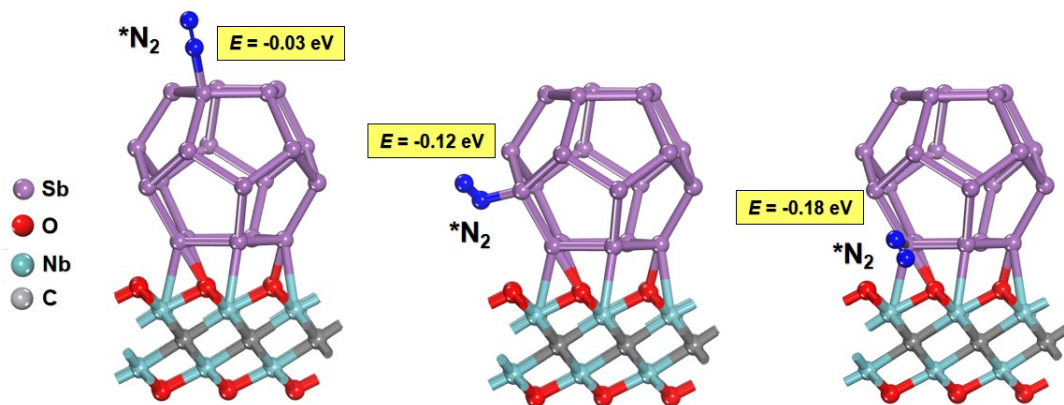
Fig. S20. Optimized structures of N_2 adsorption on various Sb sites of Sb/Nb$_2$CT$_x$ and their corresponding N_2 adsorption energy (E).
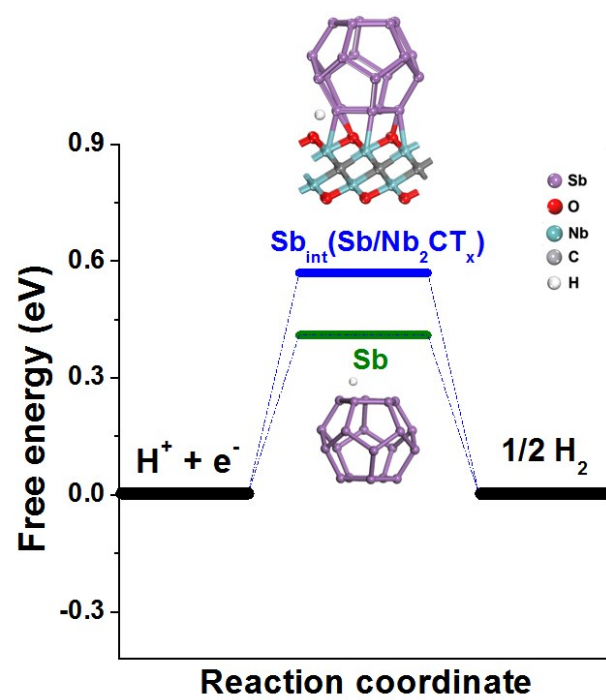
Fig. S21. Free energies of H adsorption (G_{*H}) on Sb and Sb_{int} (Sb/Nb_2CT_x).

Table S1. Comparison of the optimum NH$_3$ yield and Faradic efficiency (FE) for recently reported MXene-based NRR electrocatalysts at ambient conditions

Catalyst	Electrolyte	Potential (V vs RHE)	NH$_3$ yield rate (μg h^{-1} mg^{-1})	FE(%)	Ref.
TiO$_2$/Ti$_3$C$_2$T$_x$	0.1 M HCl	-0.55	32.17	16.07	[18]
Ti$_3$C$_2$T$_x$ QDs	0.1 M HCl	-0.5	62.94	13.3	[19]
Ti$_3$C$_2$T$_x$ nanosheets	0.1 M HCl	-0.4	20.4	9.3	[20]
Fe$_2$O$_3$/Ti$_3$C$_2$T$_x$	0.05 M H$_2$SO$_4$	-0.2	21.9	25.44	[21]
TiO$_2$/Ti$_3$C$_2$T$_x$	0.1 M HCl	-0.60	26.32	8.42	[22]
Mn$_3$O$_4$/Ti$_3$C$_2$T$_x$	0.1 M Na$_2$SO$_4$	-0.5	25.95	5.51	[23]
1T-MoS$_2$/Ti$_3$C$_2$	0.1 M HCl	-0.3	30.33	10.94	[24]
Single-atom Ru/Mo$_2$CT$_x$	0.5 m K$_2$SO$_4$	-0.3	40.57	25.77	[25]
Fluorine-Free Ti$_3$C$_2$T$_x$ Nanosheets	0.1 M HCl	-0.3	36.9	9.1	[26]
MnO$_2$/Ti$_3$C$_2$T$_x$	0.1 M HCl	-0.55	34.12	11.39	[27]
Sb/Nb$_2$CT$_x$	0.5 M LiClO$_4$	-0.4	49.8	27.3 (-0.2 V)	This wok

Supplementary references

[1]. R. Zhao, H. Di, C. Wang, X. Hui, D. Zhao, R. Wang, L. Zhang and L. Yin, *ACS Nano*, 2020, **14**, 13938-13951.

[2]. Y. Liu, Y. Luo, Q. Li, J. Wang and K. Chu, *Chem. Commun.*, 2020, **56**, 10227-10230.

[3]. W. Gu, Y. Guo, Q. Li, Y. Tian and K. Chu, *ACS Appl. Mater. Inter.*, 2020, **12**, 37258-37264.

[4]. K. Chu, Y. Liu, Y. Chen and Q. Li, *J. Mater. Chem. A*, 2020, **8**, 5200-5208.

[5]. D. Zhu, L. Zhang, R. E. Ruther and R. J. Hamers, *Nat. Mater.*, 2013, **12**, 836.

[6]. G. W. Watt and J. D. Chrisp, *Anal. Chem.*, 1952, **24**, 2006-2008.

[7]. Y. Tian, X. Shao, M. Zhu, W. Liu, Z. Wei and K. Chu, *Dalton T.*, 2020, **49**, 12559-12564.

[8]. P. Shen, Y. Liu, Q. Li and K. Chu, *Chem. Commun.*, 2020, **56**, 10505-10508

[9]. Q. Li, Y. Cheng, X. Li, Y. Guo and K. Chu, *Chem. Commun.*, 2020, **56**, 13009-13012.

[10]. B. Hu, M. Hu, L. C. Seefeldt and T. L. Liu, *ACS Energy Lett.*, 2019, **4**, 1053-1054.

[11]. S. J. Clark, M. D. Segall, C. J. Pickard, P. J. Hasnip, M. I. J. Probert, K. Refson and M. C. Payne, *Z. Kristallogr.*, 2005, **220**, 567-570.

[12]. A. A. Peterson, *Energy Environ. Sci.*, 2010, **3**, 1311-1315.

[13]. H. Xin, A. Vojvodic, J. Voss, J. K. Nørskov and F. Abild-Pedersen, *Phys. Rev. B*, 2014, **89**, 115114.

[14].   X. Li, T. Li, Y. Ma, Q. Wei, W. Qiu, H. Guo, X. Shi, P. Zhang, A. M. Asiri and L. Chen, *Adv. Energy. Mater.*, 2018, **8**, 1801357.

[15].   J. Q. Tian, Q. Liu, A. M. Asiri and X. P. Sun, *J. Am. Chem. Soc.*, 2014, **136**, 7587-7590.

[16].   J. Han, Z. Liu, Y. Ma, G. Cui, F. Xie, F. Wang, Y. Wu, S. Gao, Y. Xu and X. Sun, *Nano Energy*, 2018, **52**, 264-270.

[17].   L. C. Green, D. A. Wagner, J. Glogowski, P. L. Skipper, J. S. Wishnok and S. R. Tannenbaum, *Analytical biochemistry*, 1982, **126**, 131-138.

[18].   Y. Fang, Z. Liu, J. Han, Z. Jin, Y. Han, F. Wang, Y. Niu, Y. Wu and Y. Xu, *Advanced Energy Materials*, 2019, **9**.

[19].   Z. Jin, C. Liu, Z. Liu, J. Han, Y. Fang, Y. Han, Y. Niu, Y. Wu, C. Sun and Y. Xu, *Advanced Energy Materials*, 2020, **10**.

[20].   J. Zhao, L. Zhang, X.-Y. Xie, X. Li, Y. Ma, Q. Liu, W.-H. Fang, X. Shi, G. Cui and X. Sun, *Journal of Materials Chemistry A*, 2018, **6**, 24031-24035.

[21].   Y. Guo, T. Wang, Q. Yang, X. Li, H. Li, Y. Wang, T. Jiao, Z. Huang, B. Dong, W. Zhang, J. Fan and C. Zhi, *ACS Nano*, 2020, **14**, 9089-9097.

[22].   J. Zhang, L. Yang, H. Wang, G. Zhu, H. Wen, H. Feng, X. Sun, X. Guan, J. Wen and Y. Yao, *Inorg Chem*, 2019, **58**, 5414-5418.

[23].   C. Wang, X.-D. Zhu and P.-J. Zuo, *Chemical Engineering Journal*, 2020, **396**.

[24].   X. Xu, B. Sun, Z. Liang, H. Cui and J. Tian, *ACS Appl Mater Interfaces*, 2020, **12**, 26060-26067.

[25].   W. Peng, M. Luo, X. Xu, K. Jiang, M. Peng, D. Chen, T. S. Chan and Y. Tan, *Advanced Energy Materials*, 2020, **10**.

[26].   T. Li, X. Yan, L. Huang, J. Li, L. Yao, Q. Zhu, W. Wang, W. Abbas, R. Naz, J. Gu, Q. Liu, W. Zhang and D. Zhang, *Journal of Materials Chemistry A*, 2019, **7**, 14462-14465.

[27].   W. Kong, F. Gong, Q. Zhou, G. Yu, L. Ji, X. Sun, A. M. Asiri, T. Wang, Y. Luo and Y. Xu, *J. Mater. Chem. A*, 2019, **7**, 18823-18827.